Available online at www.sciencedirect.com
ScienceDirect
Trans. Nonferrous Met. Soc. China 35(2025) 3272−3287
Transactions of Nonferrous Metals Society of China
www.tnmsc.cn

Effect of extrusion temperature on dynamic recrystallization behavior and mechanical properties of flame-retardant Mg−Al−Ca−Zn−Sn−Mn alloy

Xi-zao WANG[1,2], Tian-jiao LUO[1], Qiu-yan HUANG[1],
Tian-yu LIU[1,2], Ying-ju LI[1], Ce ZHENG[1], Shuang GUO[1,3], Yuan-sheng YANG[1]

1. Institute of Metal Research, Chinese Academy of Sciences, Shenyang 110016, China;
2. School of Materials Science and Engineering, University of Science and Technology of China, Shenyang 110016, China;
3. School of Materials Science and Engineering, Shenyang University of Technology, Shenyang 110870, China

Received 27 January 2024; accepted 2 September 2024

Abstract: The effect of extrusion temperature on the dynamic recrystallization behavior and mechanical properties of the flame-retardant Mg−6Al−3Ca−1Zn−1Sn−Mn (wt.%) alloy was investigated. The observed dynamic recrystallization mechanisms in the alloy include continuous dynamic recrystallization (CDRX) and particle simulated nucleation (PSN) during hot extrusion. A significant increase in yield strength, from 218 to 358 MPa, representing a 140 MPa increase, is achieved by decreasing the extrusion temperature. The strengthening mechanisms were analyzed quantitatively, with the enhanced strength primarily attributed to grain boundary and dislocation strengthening. The plasticity mechanism was analyzed qualitatively, and the increase in the volume fraction of unDRXed grains caused by the decrease in extrusion temperature leads to an increase in the number of $\{10\bar{1}2\}$ tensile twins during the tensile deformation, resulting in a reduction in plasticity.

Key words: flame-retardant magnesium alloys; PSN mechanism; high strength; hot extrusion

1 Introduction

Low-cost flame-retardant Mg−Al−Ca−(Mn) alloys have attracted extensive attention for their high strength [1,2]. For example, XU et al [3] reported that an as-extruded Mg−3.5Al−3.3Ca−0.4Mn (wt.%) alloy exhibits a high tensile yield strength of 410 MPa, which is attributed to fine dynamically recrystallized grains and a strong basal texture. LI et al [4] successfully developed a high-strength as-extruded Mg−2.7Al−3.5Ca−0.4Mn (wt.%) alloy with a tensile yield strength of 437 MPa. Moreover, the effect of Zn and Sn additions on the microstructure and mechanical properties of Mg alloys has also attracted much attention [5−7]. BIAN et al [8,9] found that the addition of Zn significantly enhanced the room temperature formability of the Mg−1.1Al−0.3Ca−0.2Mn (wt.%) alloy due to the development of a weaken basal texture. HOSEINIATHAR et al [10] reported that the addition of Zn delayed the dynamic recrystallization of Mg−2Gd (wt.%) alloy. WANG et al [5] found that Sn effectively improved the strength and ductility of Mg−6Al−4Zn (wt.%) alloy. The co-addition of Zn and Sn also affects the microstructure and mechanical properties of Mg alloys. LIU et al [11] reported that the strength and ductility of the Mg−1Sb−1Mn (wt.%) alloy were simultaneously improved by the co-addition of Zn and Sn. In a word, the addition of Zn and Sn significantly affects the microstructure and the

Corresponding author: Yuan-sheng YANG, Tel: +86-24-23844528, E-mail: ysyang@imr.ac.cn
https://doi.org/10.1016/S1003-6326(25)66880-4

mechanical properties of Mg alloys [12,13]. However, there have been few systematic studies on the influence of co-adding of Zn and Sn on the microstructure and mechanical properties of flame-retardant Mg−Al−Ca−Mn alloys.

The microstructure and mechanical properties of Mg alloys are significantly influenced by the extrusion temperature, in addition to alloying [14,15]. LV et al [16] developed the as-extruded Mg−6Zn−2Yb−0.5Zr (wt.%) alloy with a good ultimate tensile strength of 370 MPa by adjusting the extrusion temperature, attributed to grain boundary strengthening and strong texture. CHA and PARK [17] reported that the tensile yield strength of the Mg−3Al−1Zn−0.3Mn (wt.%) alloy was enhanced with increasing the extrusion temperature, due to strong texture hardening and strain hardening. YANG et al [18] found that the as-extruded Mg−8Gd−4Y−1Mn−0.4Sc (wt.%) alloy exhibited an ultimate tensile strength of 425 MPa and a tensile yield strength of 352 MPa at an extrusion temperature of 400 °C. They also noted that the average size and volume fraction of DRXed grains of Mg−8Gd−4Y−1Mn−0.4Sc (wt.%) alloy increased with increasing extrusion temperature, while the yield tensile strength decreased. It is evident from previous results that the extrusion temperature has a significant effect on the microstructure and mechanical properties of Mg alloys [15,16]. However, there is limited research focusing on the effect of extrusion temperature on the microstructure and mechanical properties of flame-retardant Mg−Al−Ca−Mn alloys containing Zn and Sn. It is important to study the effect of co-adding of Zn and Sn elements on flame-retardant Mg−Al−Ca−Mn alloys and extrusion temperature on Mg−Al−Ca−Mn−Zn−Sn alloys, which is of great significance to further promote the application of flame-retardant Mg−Al−Ca−Mn alloys. In addition, exploring the dynamic recrystallization behavior of these alloys at different extrusion temperatures and establishing the correlation between microstructures and mechanical properties of flame-retardant alloys are crucial for the development of new flame-retardant alloys.

This study presents the preparation of a high ignition point and high strength Mg−6Al−3Ca−Mn−1Zn−1Sn (wt.%) alloy. The strength of the alloy was improved significantly by controlling the extrusion temperature. Dynamic recrystallization mechanism of the alloy was analyzed, and both the quantitative analysis of the strengthening mechanism and qualitative analysis of the plasticity mechanism were conducted. These analyses offer fresh perspectives on producing cost-effective flame-retardant Mg−Al−Ca−Mn alloys with high strength.

2 Experimental

Mg−6Al−3Ca−Mn−1Zn−1Sn (wt.%) alloy was prepared using commercially pure Mg (99.95%), Al (99.95%), Zn (99.95%), Mg− 20wt.%Ca master alloy, and Mg−10wt.%Mn master alloy. The alloy was fabricated via gravity casting under CO_2 and SF_6 gas protection. The as-cast ingot was then heated at 500 °C for 48 h, followed by hot extrusion at 350, 320, and 290 °C with an extrusion ratio of 10∶1, and extrusion speed of 0.5−1 mm/s. The as-extruded samples were denoted as ZS-350, ZS-320, and ZS-290, respectively, based on their extrusion temperatures.

The microstructure of the experimental samples was examined using various techniques, including optical microscopy (OM), scanning electron microscopy (SEM) with an energy disperse spectrometry (EDS), X-ray diffractometry (XRD), and transmission electron microscopy (TEM) operating at 200 kV. Additionally, the electron backscattered diffraction (EBSD) analysis was conducted on an FEI/Nova SEM equipped with an HKL Channel 5 system, with a step size of 0.4 μm. The OM, SEM, and EDS samples were observed after mechanical polishing and etching in a mixed solution (14 mL alcohol, 2 mL purified acetic acid, and 1 g picric acid). The XRD samples were observed after mechanical polishing. The EBSD samples were observed after mechanical polishing and electrolytic polishing. Tensile tests were performed on an AG-Xplus100KN tensile machine at room temperature, with the test samples having a gauge length of 25 mm and a diameter of 5 mm.

3 Results

3.1 Microstructure characterizations

The microstructures of the three experimental samples were initially observed using OM (Fig. 1). These alloys exhibit a bimodal microstructure, consisting of coarse unDRXed grains elongated

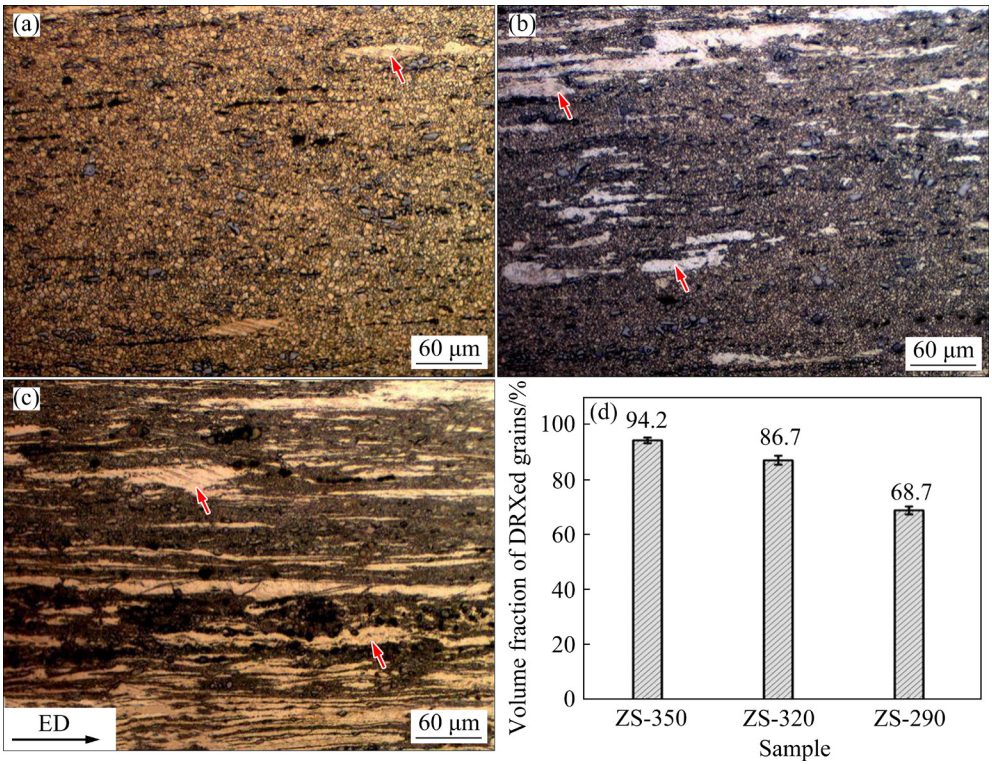

Fig. 1 OM images of ZS-350 (a), ZS-320 (b) and ZS-290 (c) alloys after extrusion, and volume fractions of DRXed grains of experimental alloys (d) (The red arrows represent the unDRXed grains of alloys)

along the extrusion direction and fine DRXed grains. The volume fractions of DRXed grains in each of the three experimental alloys were calculated using Image Pro Plus. The calculated volume fractions of DRXed grains for the ZS-350, ZS-320, and ZS-290 alloys are 94.2%, 86.7%, and 68.7%, respectively. These values suggest that decreasing the extrusion temperature has a detrimental effect on the volume fraction of DRXed grains. Furthermore, it is observed that the volume fraction of DRXed grains in the ZS-290 alloy exhibits a significant decrease in comparison to the ZS-350 and ZS-320 alloys.

Figures 2(a−c) show the EBSD inverse pole figures (IPF) of the three experimental alloys. In these figures, the low angle grain boundaries (LAGBs, <15°) are represented by white lines, while the high angle grain boundaries (HAGBs, >15°) are shown by black lines. Figures 2(d−f) show the bond contrast maps of the experimental alloys. It can be seen that the location of the bulk second phase particles in Figs. 2(d−f) corresponds to the white area in the IPF maps, so the white areas in Figs. 2(a−c) represent the second phase particles. The alloys exhibit a bimodal microstructure, consisting of coarse unDRXed grains with a single orientation and fine DRXed grains with a random orientation in all three experimental alloys. In the three experimental alloys, despite the different extrusion temperatures, the unDRXed grains exhibit a similar orientation with $[10\bar{1}0]$ parallel to the extrusion direction and many LAGBs are observed in the unDRXed grains. The average sizes of the DRXed grains of ZS-350, ZS-320, and ZS-290 alloys are 2.53, 2.22, and 1.82 μm, respectively. This observation suggests that decreasing the extrusion temperature results in a reduction in the size of the DRXed grains.

Figure 3 shows TEM images of unDRXed grains and DRXed grains of ZS-350, ZS-320, and ZS-290 alloys. The presence of numerous low angle grain boundaries (LAGBs) in the unDRXed grains aligns with the findings from the EBSD results displayed in Fig. 2. The spacings of the LAGBs in the ZS-350, ZS-320, and ZS-290 alloys range 800−850, 300−350, and 260−400 nm, respectively. A decreasing trend in the LAGBs spacing is observed as the extrusion temperature decreases. The average sizes of DRXed grains of ZS-350, ZS-320, and ZS-290 alloys are 2.07, 2.01, and

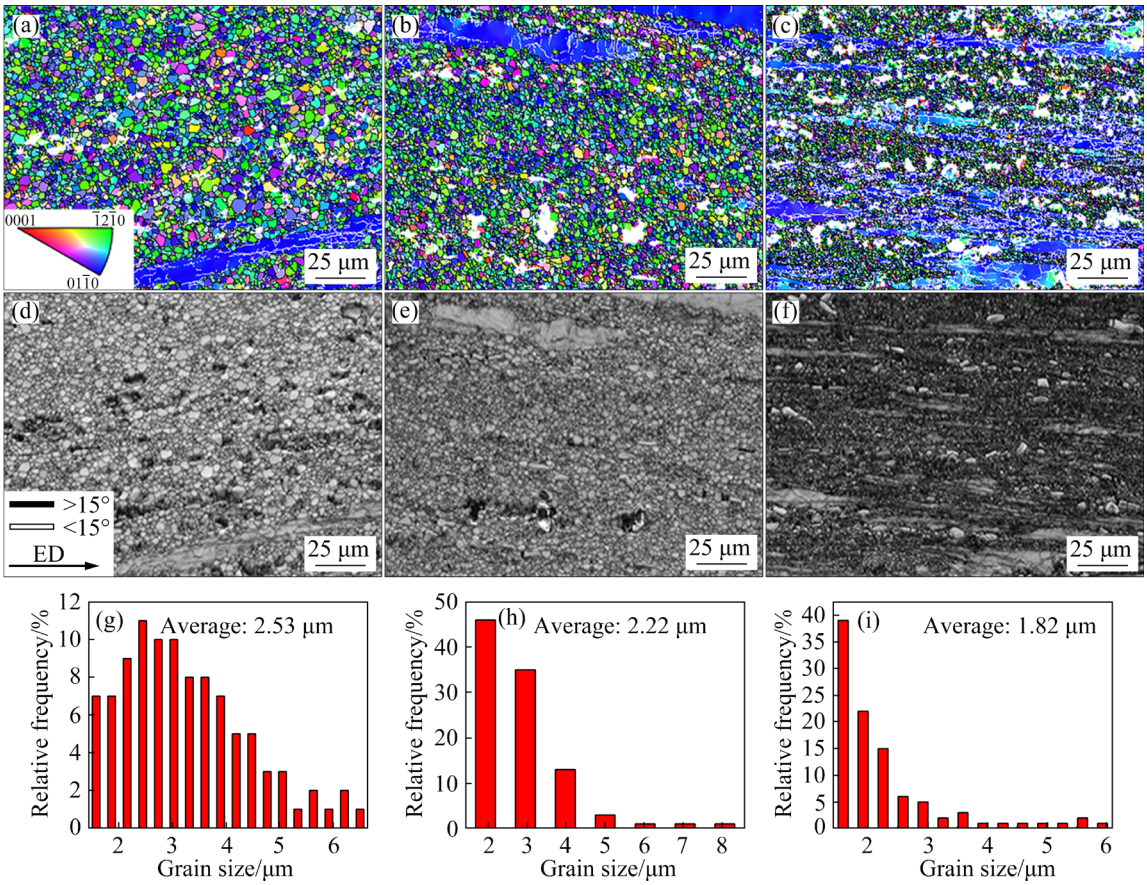

Fig. 2 EBSD inverse pole figures (IPF) of ZS-350 (a), ZS-320 (b), and ZS-290 (c) alloys (White bulks represent the second phase particles); Bond contrast maps of ZS-350 (d), ZS-320 (e), and ZS-290 (f) alloys (White lines represent the LAGBs (low-angle grain boundary), and black lines represent the HAGBs (high-angle grain boundary)); Average sizes of DRXed grains of ZS-350 (g), ZS-320 (h), and ZS-290 (i) alloys

0.78 μm, respectively. These sizes are slightly smaller than those derived from the EBSD results, potentially attributed to challenges in detecting DRXed grains of approximately 1 μm in size. It is evident that as the extrusion temperature decreases, the average sizes of both DRXed grains and unDRXed grains decrease in a similar trend. Nano-precipitates have been observed in DRXed grains of ZS-320 and ZS-290 alloys, which are similar to those found in Mg−5.5Al−3Ca−0.3Mn (wt%) alloy and can be identified as Al_8Mn_5 precipitates [19]. However, these precipitates are not detected in DRXed grains of ZS-350 alloy. LI et al [20] reported that Al_8Mn_5 phase is dissolved into the matrix when annealed at 350 °C, which explains the absence of Al_8Mn_5 precipitates in DRXed grains of ZS-350 alloy.

Figure 4 shows the KAM maps and misorientation angles of the three experimental alloys. The color representations in the KAM maps and the associated KAM values serve as indicators of the residual dislocation density within the alloys [21]. The residual dislocations are predominantly observed in the unDRXed grains, with minimal presence in the DRXed grains. The KAM values for the ZS-350, ZS-320, and ZS-290 alloys are 0.45°, 0.53°, and 0.79°, respectively. These values indicate that the density of residual dislocations increases with a decrease in extrusion temperature. This trend is attributed to the rise in the volume fraction of unDRXed grains as the extrusion temperature decreases. Further analysis of the misorientation angles reveals that angles less than 15°, indicative of low angle grain boundaries (LAGBs), exhibit a higher prevalence as the extrusion temperature decreases. This observation signifies an increase in the volume fraction of unDRXed grains with decreasing extrusion temperature.

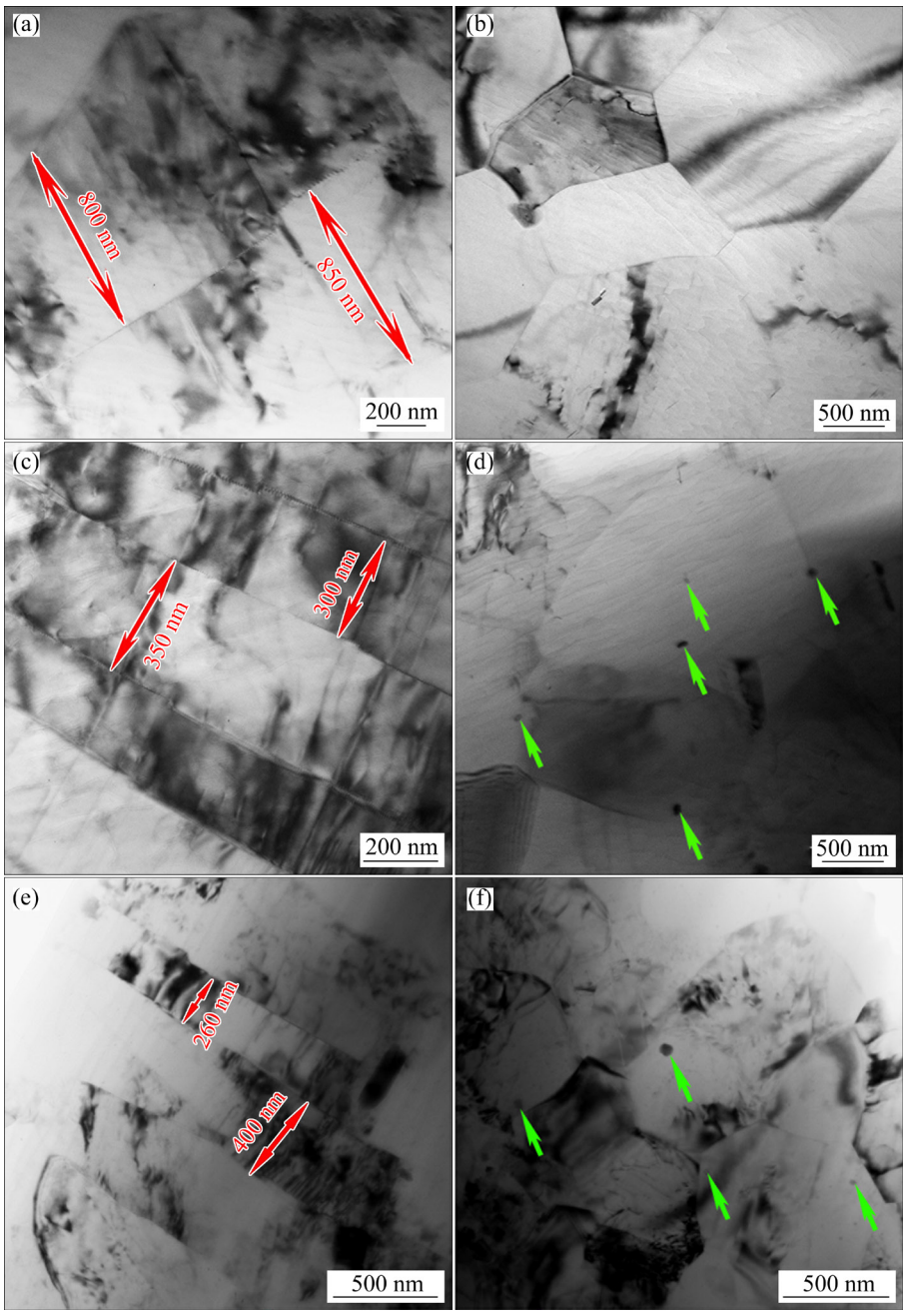

Fig. 3 TEM images of unDRXed grains (a, c, e) and DRXed grains (b, d, f) of ZS-350 (a, b), ZS-320 (c, d), and ZS-290 (e, f) alloys (Green arrows represent Al_8Mn_5 precipitates)

Figure 5 shows the secondary electron images and corresponding EDS maps. The second phase particles are distributed along the extrusion direction and the average sizes of the second phase particles of ZS-350, ZS-320, and ZS-290 alloys are 5.0, 4.9, and 4.8 μm, respectively. These findings suggest a slight decrease in the average sizes of the second phase particles as the extrusion temperature decreases. The volume fraction of second phase particles remains consistent at approximately 12%, as the composition remains unchanged. The elements Al, Ca, Mn, and Sn are found to be distributed in the second phase particles, while Zn is predominantly distributed in the matrix. To identify the types of phases, an XRD measurement was carried out (Fig. 6). The three experimental alloys all contain the same types of phases, including α-Mg phase, Al_2Ca phase, CaMgSn phase, and Al_8Mn_5 phase. This indicates that altering the extrusion temperature does not affect the types of second phase particles present. Further, the composition of the second phase particles marked

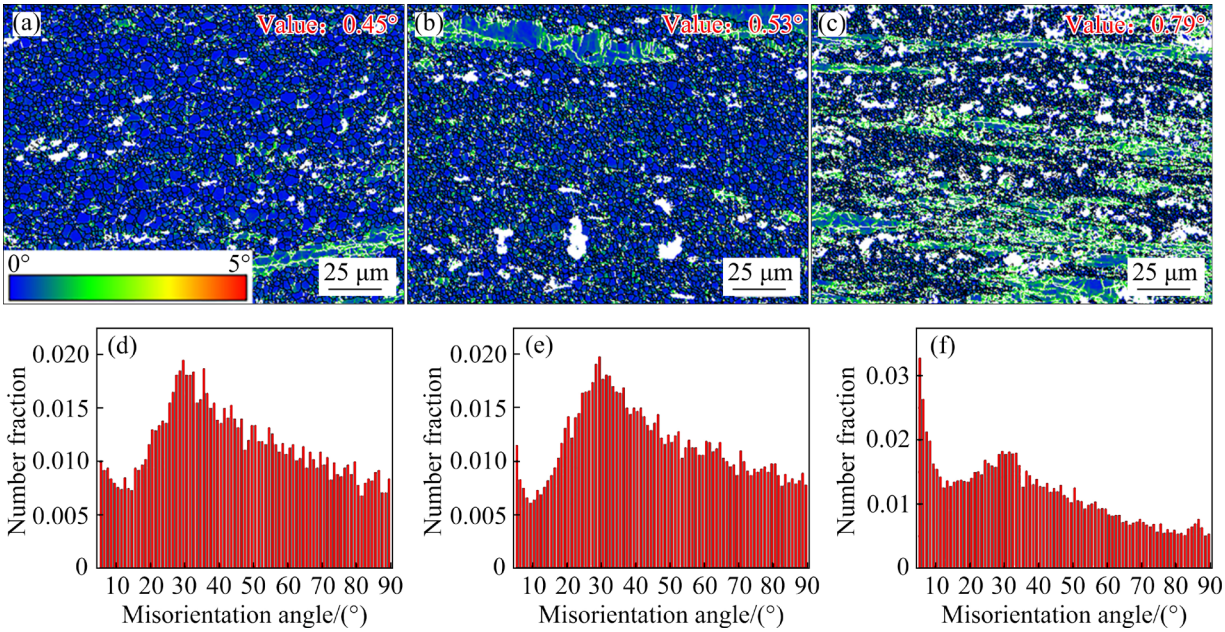

Fig. 4 KAM maps (a−c) and misorientation angle distributions (d−f) of ZS-350 (a, d), ZS-320 (b, e), and ZS-290 (c, f) alloys (White bulks represent the second phase particles)

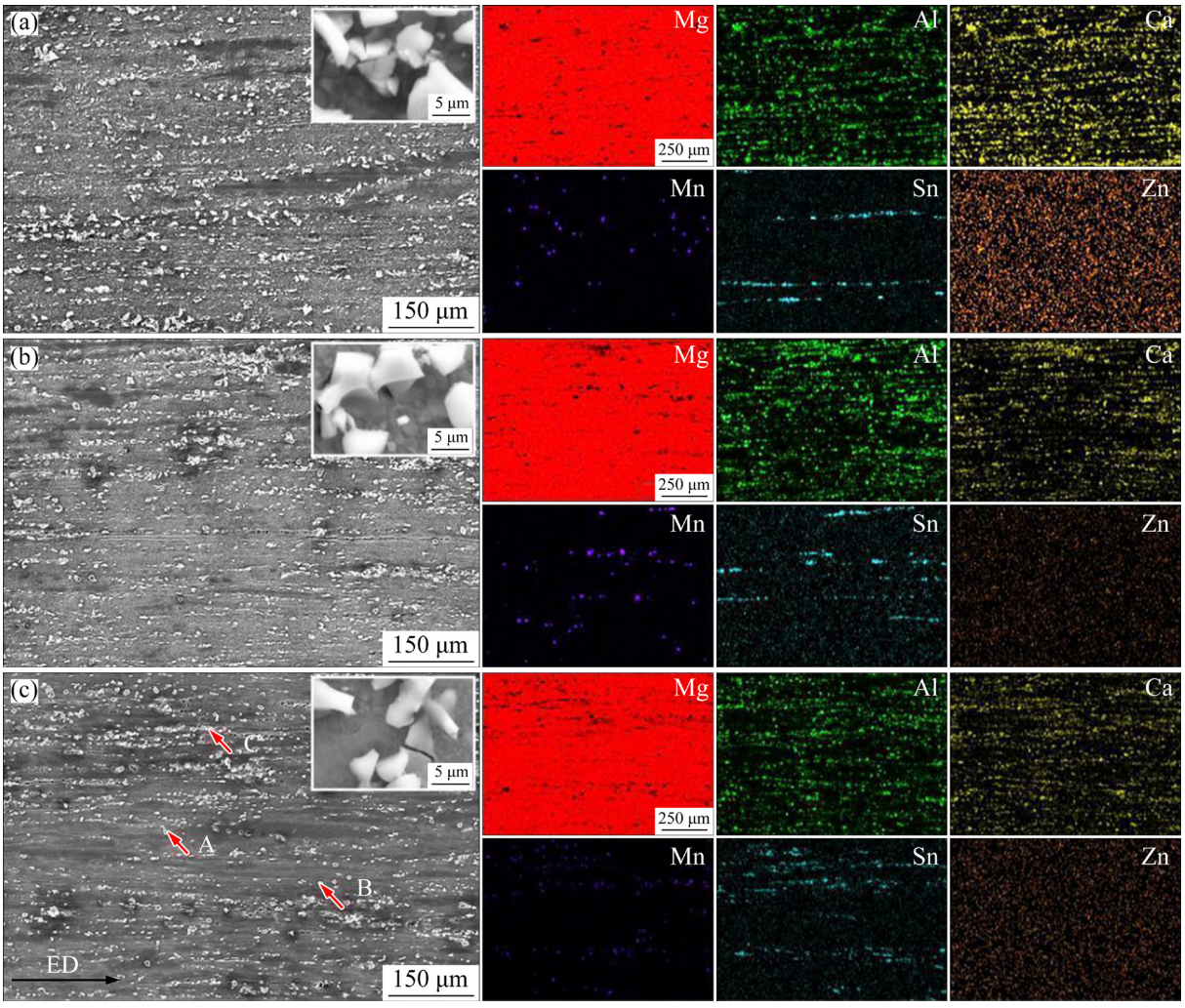

Fig. 5 Secondary electron images and corresponding EDS maps of ZS-350 (a), ZS-320 (b) and ZS-290 (c) alloys

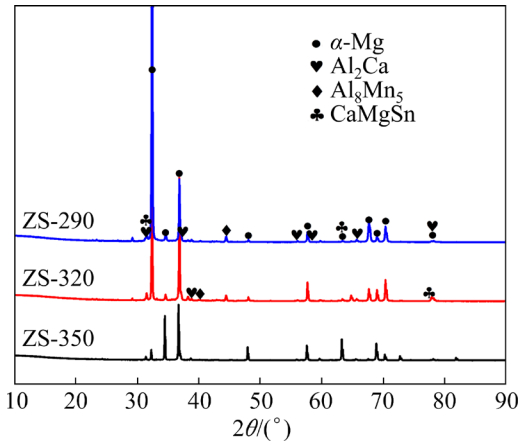

Fig. 6 X-ray diffraction patterns of three experimental alloys

by the red clippings in Fig. 5(c) were examined, as shown in Table 1. At Point A, the molar ratio of Al to Ca is about 2∶1, which can be identified as Al_2Ca phase particle, so the second phase particles enriched with Al and Ca atoms are Al_2Ca (Fig. 5). At Point B, the molar ratio of Al to Mn is about 8∶5, which can be identified as Al_8Mn_5 phase particle, so the second phase particles enriched with Al and Mn atoms are Al_8Mn_5 (Fig. 5). At Point C, the molar ratio among Ca, Mg, and Sn is about 1∶1∶1, which can be identified as CaMgSn phase particle, so the second phase particles enriched with Ca, Mg, and Sn atoms are CaMgSn (Fig. 5).

Table 1 Composition of second phase particles marked by red clippings in Fig. 5(c) (at.%)

Point	Mg	Al	Ca	Mn	Zn	Sn
A	8.21	60.33	31.37	0.02	0.03	0.03
B	14.96	52.3	0.03	32.69	0.01	0.01
C	35.07	1.70	29.92	0.02	0.03	33.23

3.2 Texture

It can be seen from Fig. 2 that the fine DRXed grains have a relatively random texture, whereas the coarse unDRXed grains exhibit a texture with $\langle 10\bar{1}0 \rangle$ planes parallel to the extrusion direction. The textures of the three experimental alloys have a significant effect on their mechanical properties [22]. Figure 7 shows the PFs of different regions of

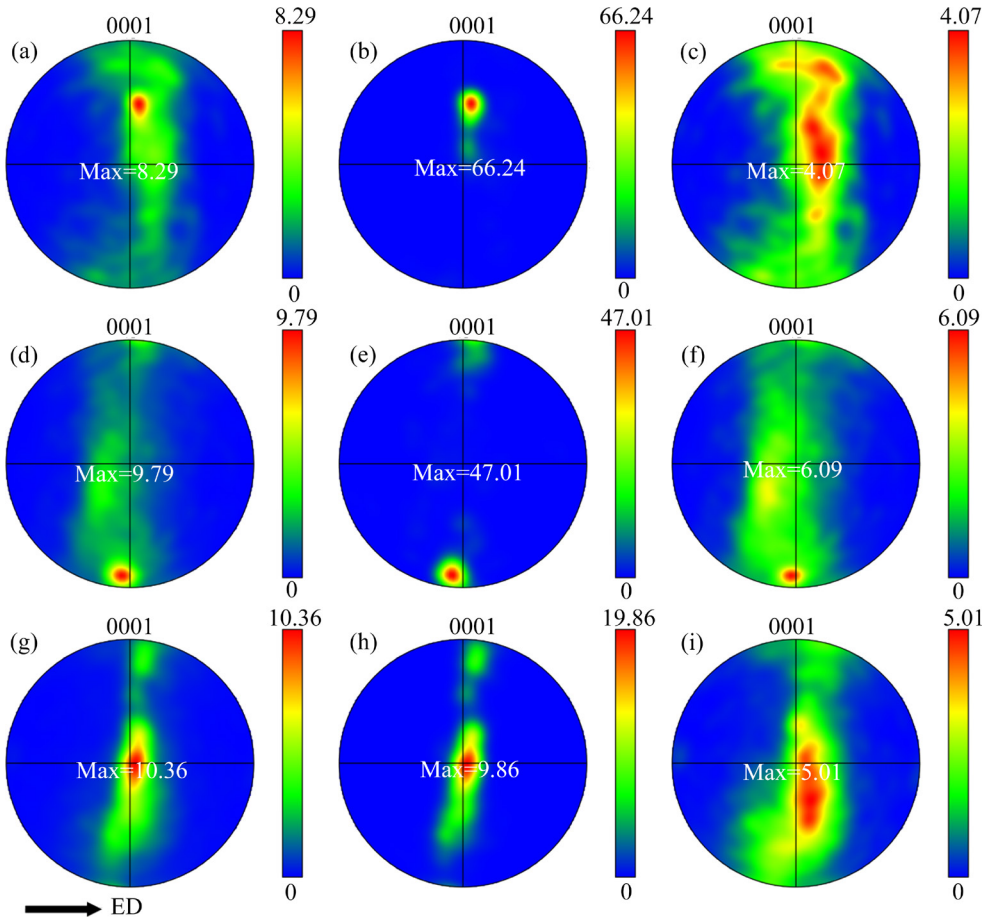

Fig. 7 PFs of grains in ZS-350 (a−c), ZS-320 (d−f) and ZS-290 (g−i) alloys: (a, d, g) All grains; (b, e, h) UnDRXed grains; (c, f, i) DRXed grains

the three experimental alloys. It is evident that all three alloys showcase a typical extrusion basal fiber texture, where the basal plane aligns parallel to the extrusion direction. The textures within the unDRXed grains of the alloys are notably strong, while the DRXed grains exhibit a weaker texture. The intensity of the texture increases as the extrusion temperature decreases. This trend can be attributed to the rise in volume fraction of unDRXed grains exhibiting a strong basal texture as the extrusion temperature decreases.

Figure 8 shows the distributions of Schmid factors of $\{0001\}\langle 11\bar{2}0\rangle$ slip of three experimental alloys. It is observed that the unDRXed grains display low Schmid factors, while the DRXed grains exhibit high Schmid factors. This implies that basal slip is more likely to occur in DRXed grains, and the unDRXed grains contribute to higher yield strength [23]. The average Schmid factors for the ZS-350, ZS-320, and ZS-290 alloys are 0.23, 0.22, and 0.16, respectively. These values indicate that the Schmid factors decrease as the extrusion temperature decreases. This decrease is attributed to the increase in the volume fraction of unDRXed grains with the extrusion temperature, where the unDRXed grains show lower Schmid factors compared to the DRXed grains.

Figure 9 shows the inverse pole figures (IPF) of DRXed grains of ZS-350, ZS-320, and ZS-290 alloys. In the case of the ZS-350 alloy, the intensity on the inverse pole figures is distributed between the $\langle 11\bar{2}0\rangle$ and $\langle 10\bar{1}0\rangle$ poles. As the extrusion temperature decreases, the intensity of the $\langle 10\bar{1}0\rangle$ pole gradually increases while the intensity of the $\langle 11\bar{2}0\rangle$ pole gradually decreases, indicating that a gradual shift in texture from the $\langle 11\bar{2}0\rangle$ component to the $\langle 10\bar{1}0\rangle$ component. The intensity of the DRXed grains increases with decreasing extrusion temperature, which correlates with the reduction in the size of the DRXed grains. LI et al [4] have also reported this phenomenon, where larger DRXed grains exhibit more $\langle 11\bar{2}0\rangle$ texture component. The ZS-350 alloy has the largest DRXed grain size, resulting in a stronger $\langle 11\bar{2}0\rangle$ texture component and a weaker texture overall.

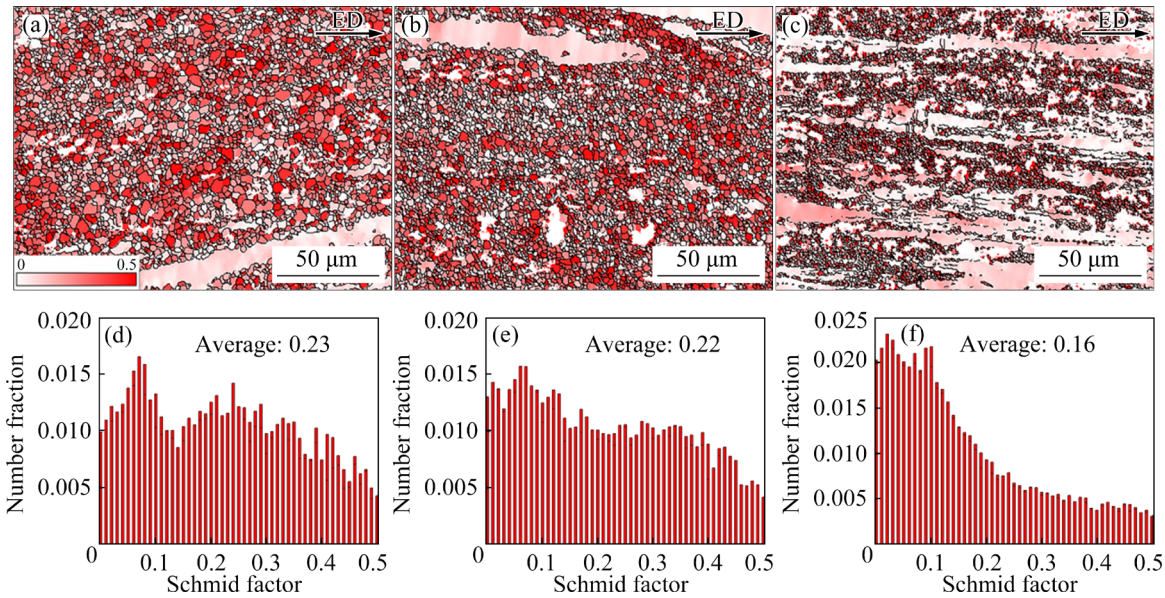

Fig. 8 Distributions of Schmid factors of $\{0001\}\langle 11\bar{2}0\rangle$ slip of ZS-350 (a, d), ZS-320 (b, e), and ZS-290 (c, f) alloys

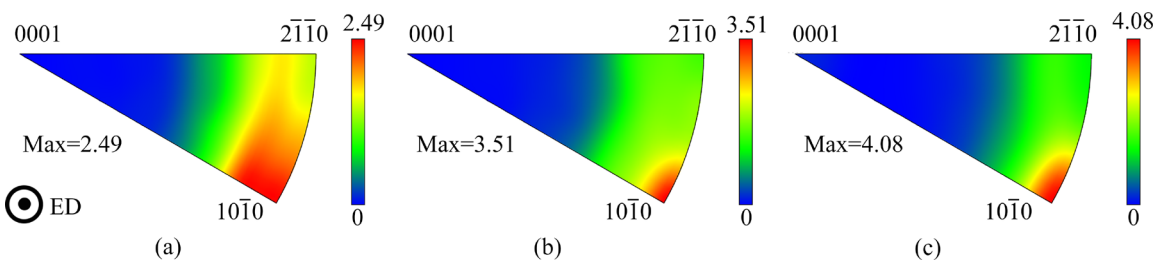

Fig. 9 Inverse pole figures (IPF) in ED of DRXed grains of ZS-350 (a), ZS-320 (b), and ZS-290 (c) alloys

3.3 Mechanical properties

Figures 10(a, b) and Table 2 present the yield strength (YS), ultimate tensile strength (UTS), and elongation to failure (EL) of ZS-350, ZS-320, and ZS-290 alloys. The ZS-350 alloy exhibits a yield strength (YS) of 218 MPa, an ultimate tensile strength (UTS) of 298 MPa, and an elongation to failure (EL) of 12.8%, respectively. These values indicate medium strength and high elongation, with the highest elongation among the 3Ca-containing Mg alloys. The ZS-320 alloy exhibits a yield strength (YS) of 246.3 MPa, an ultimate tensile strength (UTS) of 312 MPa, and an elongation to failure (EL) of 12.2%, respectively. In comparison, the ZS-320 alloy has a higher yield strength and slightly decreased elongation. The ZS-290 alloy exhibits high strength with a yield strength (YS) of 358.6 MPa, an ultimate tensile strength (UTS) of 387.7 MPa, and an elongation to failure (EL) of 4.3%, respectively. Compared to ZS-350 alloy, the yield strength (YS) of ZS-290 alloy is significantly increased by 140 MPa, and compared to ZS-320 alloy, the yield strength (YS) of ZS-290 alloy is significantly increased by 112 MPa. It is generally observed that the strength of alloys is enhanced by decreasing the extrusion temperature. However, this is at the expense of a significant reduction in the elongation to failure (EL), which is only 4.3%. Figure 10(c) shows the heating curve of the ZS-290 alloy to illustrate the flame-retardant properties. When the heating curve starts to rise sharply it proves that the sample is burning. It can be seen that the ZS-290 alloy does not burn at 1058 °C, indicating that the ZS-290 alloy has excellent flame-retardant properties.

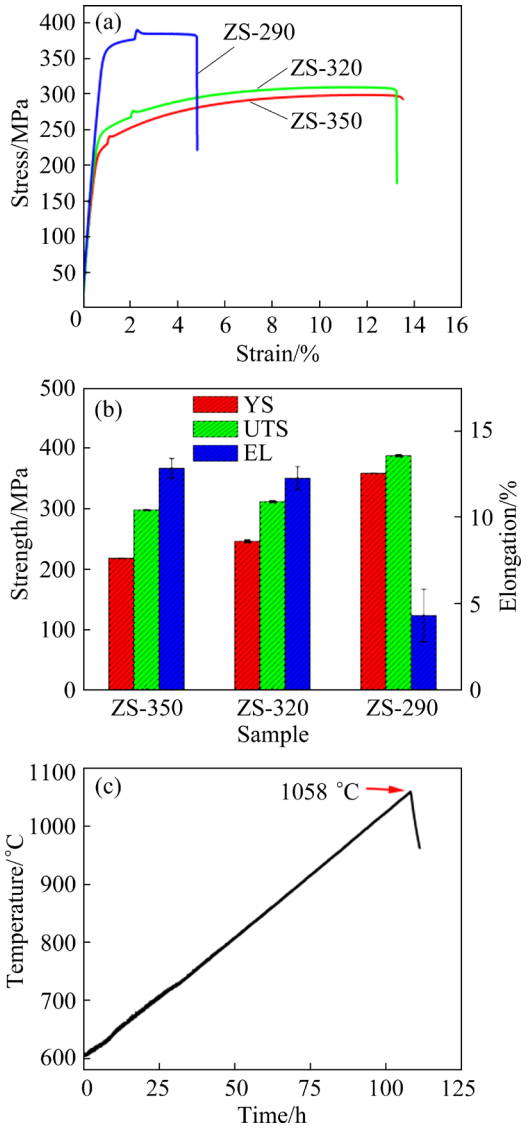

Fig. 10 Engineering tensile stress−train curves (a) and mechanical properties (b) of ZS-350, ZS-320, and ZS-290 alloys; Heating curve of ZS-290 alloy (c)

Table 2 Mechanical properties of ZS-350, ZS-320, and ZS-290 alloys

Alloy	YS/MPa	UTS/MPa	EL/%
ZS-350	218±0.5	298±1	12.8±0.6
ZS-320	246.3±2.5	312±2	12.2±0.6
ZS-290	358.6±0.5	387.7±2.08	4.3±1.5

4 Discussion

4.1 Dynamic recrystallization behavior and mechanism

To analyse the dynamic recrystallization behavior and mechanism of ZS-350, ZS-320, and ZS-290 alloys during the hot extrusion, the EBSD results of the characteristic areas are selected for analysis (Fig. 11). The characteristic areas include coarse unDRXed grains with a single orientation, fine DRXed grains with random orientation, and second phase particles (Figs. 11(a−c)). Figures 11(d−f) show the phase distribution maps of ZS-350, ZS-320, and ZS-290 alloys. The location of the Al_2Ca phase particles in the distribution maps corresponds to the white areas in the IPF maps displayed in Figs. 11(a−c). The unDRXed grains in the ZS-350, ZS-320, and ZS-290 alloys are observed to contain a significant number of low angle grain boundaries (LAGBs) (Figs. 11(a−c)) and possess a high dislocation density (Fig. 4). To determine the types of the residual dislocations,

TEM was used to characterize the unDRXed grain (Fig. 12). The results show that the residual dislocations in the unDRXed grains are basal ⟨*a*⟩ dislocations and non-basal dislocations. The accumulative misorientations from grain boundaries to grain cores are represented by the accumulative misorientations along the selected lines, L1, L2, and L3 (Fig. 11). The accumulative misorientations of ZS-350, ZS-320, and ZS-290 alloys are 4.5°, 2.7°, and 5.9°, respectively. These results indicate an increasing trend in accumulative misorientations from grain boundaries to grain cores, suggesting that both alloys exhibit continuous dynamic recrystallization (CDRX) mechanism during hot extrusion.

In general, the dynamic recrystallization behavior is influenced by the second phase particles [24]. Second phase particles larger than 1 μm promote the dynamic recrystallization, while those smaller than 1 μm inhibit the dynamic recrystallization. The average sizes of the second phase particles of ZS-350, ZS-320, and ZS-290 alloys are 5.0, 4.9, and 4.8 μm, respectively. It can be determined that the sizes of the second phase

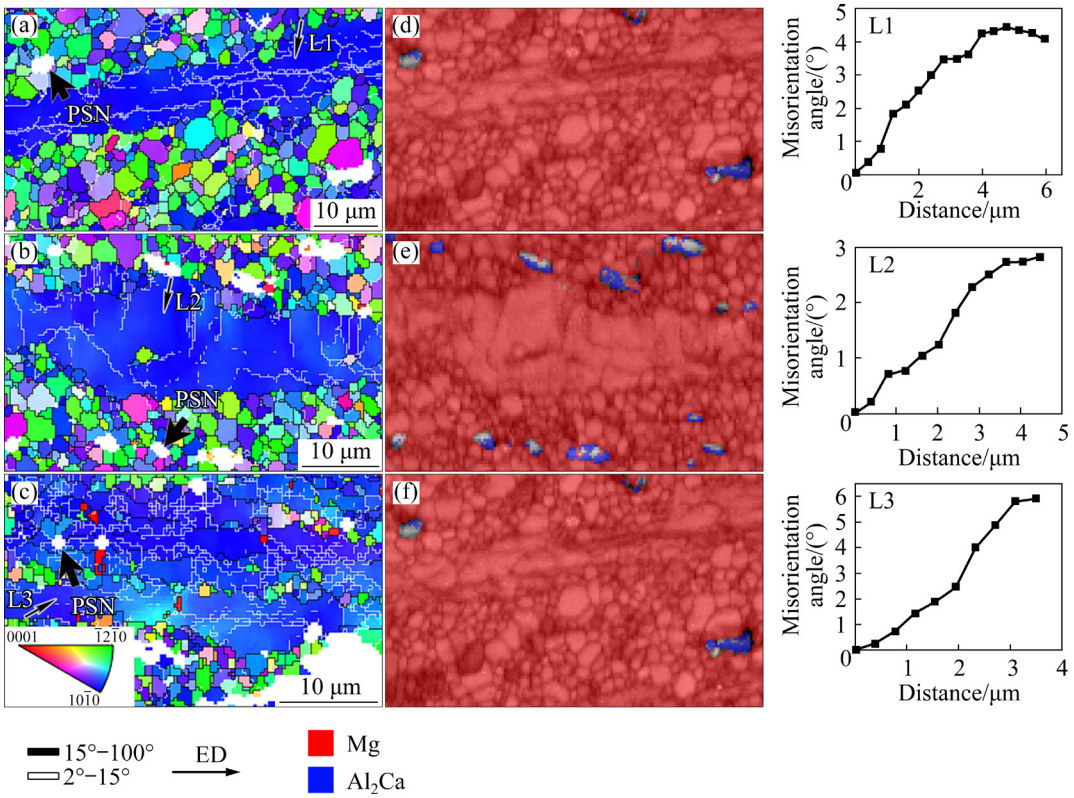

Fig. 11 EBSD inverse pole figures (IPF) of characteristic areas (a−c) and phase distribution maps (d−f) of ZS-350 (a, d), ZS-320 (b, e), and ZS-290 (c, f) alloys (White bulks represent the second phase particles)

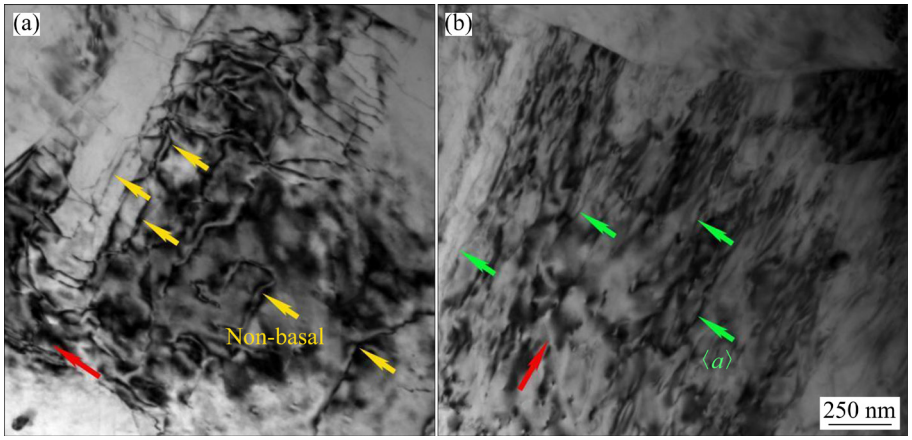

Fig. 12 TEM images of unDRXed grains: (a) ***g***=[0002]; (b) ***g***=[01$\bar{1}$0]

particles of the three experimental alloys are comparable and all are larger than 1 μm. This promotes dynamic recrystallization, which is the particle simulated nucleation (PSN) mechanism. The presence of numerous fine DRXed grains surrounding the second phase particles in the microstructure further supports PSN mechanism, where the second phase particles act as nucleation sites for dynamic recrystallization.

Based on the presented results, it can be concluded that the ZS-350, ZS-320, and ZS-290 alloys undergo continuous dynamic recrystallization (CDRX) mechanism and particle simulated nucleation (PSN) mechanism during hot extrusion. While the dynamic recrystallization mechanisms are consistent among the three experimental alloys, the volume fractions of DRXed grains vary. The comparable sizes and volume fractions of second phase particles in the three alloys suggest that the second phase particles are not the primary influencing factor. In addition, the accumulation of the basal ⟨*a*⟩ dislocations and non-basal dislocations occurs (Fig. 12), which then form the LAGBs (low angle grain boundaries) through dislocation cross-slip or climbing during the hot extrusion. Eventually, the LAGBs absorb the movable dislocations to form HAGBs (high angle grain boundaries). The movement of the dislocations is inhibited by lowering extrusion temperature, which hinders dynamic recrystallization [25]. This is why the volume fraction of DRXed grains decreases as the extrusion temperature decreases.

4.2 Strengthening and plasticity mechanisms

4.2.1 Strengthening mechanism

The strengthening mechanisms of ZS-350, ZS-320, and ZS-290 alloys after hot extrusion mainly include grain boundary strengthening, dislocation strengthening, and precipitation strengthening [26].

In the case of bimodal microstructure, the microstructures are heterogeneous, consisting of DRXed grains with random orientations and unDRXed grains with a strong texture. Therefore, the strength can be calculated using the following formula [27]:

$$\sigma_c=\sigma_1 V_1+\sigma_2 V_2 \tag{1}$$

where σ_c is the strength of Mg−Al−Ca−Mn−Zn−Sn alloy; σ_1 and σ_2 represent the strength of unDRXed grains and DRXed grains, respectively; V_1 and V_2 represent the volume fraction of unDRXed grains and DRXed grains, respectively.

The contribution of the different grains to the yield strength can be calculated using the following formula:

$$\sigma_{ys}=\sigma_{GB}+\sigma_{dislo}+\sigma_{preci} \tag{2}$$

where σ_{ys} represents the yield strength; σ_{GB} represents the strengthening contributions from grain boundary strengthening; σ_{dislo} represents the strengthening contributions from residual dislocations; σ_{preci} represents the strengthening contributions from precipitates.

(1) unDRXed grains

The contribution of the grain boundary strengthening can be calculated as follows [28]:

$$\sigma_{GB}=k_y d^{-1/2} \tag{3}$$

where k_y represents the HP-relation slope (280 MPa·μm$^{1/2}$). The contributions of the grain boundary strengthening of unDRXed grains of ZS-350, ZS-320, and ZS-290 alloys are 68, 63, and 69 MPa, respectively.

The contribution of residual dislocations strengthening can be calculated using the following formula [29]:

$$\sigma_{dislo}=M\alpha Gb\sqrt{\rho_{GND}} \tag{4}$$

where M represents Taylor factor (~2.5); α is a constant (=0.2); G is the shear modulus (~17 GPa); b is the magnitude of Burgers vector (~0.32 nm); ρ_{GND} is the density of residual dislocation and can be calculated as follows:

$$\rho_{GND}=\frac{2\Theta}{ub} \tag{5}$$

where u is equal to the scanning step length (~400 nm); Θ is evaluated from the local misorientation profile in the KAM maps (Fig. 4). According to Fig. 4, the KAM values of ZS-350, ZS-320, and ZS-290 alloys are 0.45°, 0.53°, and 0.79°, respectively. The densities of residual dislocation of ZS-350, ZS-320, and ZS-290 alloys are 7.03×10^{14}, 8.28×10^{14}, and 1.23×10^{15} m^{-2}, respectively. The calculated contributions of residual dislocation of ZS-350, ZS-320, and ZS-290 alloys are 227, 247, and 301 MPa, respectively. No nano-precipitates are observed in the unDRXed grains of ZS-350, ZS-320, and ZS-290 alloys, so $\sigma_{preci}=0$.

(2) DRXed grains

Grain boundary strengthening contributions of DRXed grains of ZS-350, ZS-320, and ZS-290 alloys are 196, 197, and 317 MPa, respectively. As the density of residual dislocations in DRXed grains is very low, σ_{dislo}=0.

The calculation for precipitation strengthening is as follows [30]:

$$\sigma = M\left(\frac{Gb}{2\pi\sqrt{1-\nu}}\right)\left(\frac{1}{\lambda}\right)\ln\left(\frac{D}{r_0}\right) \quad (5)$$

where ν is Poisson's ratio (≈0.3); λ is the effective inter-particle spacing; D is the mean particle diameter; r_0 is the dislocation core radius (~0.32 nm). No nano-precipitates are observed in the DRXed grains of ZS-350 alloy, so σ_{preci}=0. The D values of the precipitates in ZS-320 and ZS-290 alloys are 12 and 15 nm, respectively, while the λ values of the precipitates in ZS-320 and ZS-290 alloys are 280 and 300 nm, respectively. The calculated contributions of precipitation strengthening of ZS-320 and ZS-290 alloys are 34 and 33 MPa, respectively.

According to Eq. (1), the predicted strengths of ZS-350, ZS-320, and ZS-290 alloys are 202, 241, and 356 MPa, respectively. These values are slightly lower than the actual values (Fig. 10 and Table 2). This discrepancy may be due to the fact that the solid solution strengthening is not taken into account.

To better clearly reflect the effect of different strengthening mechanisms on the yield strength, the contributions of each mechanism to the yield strength are calculated (Fig. 13). The difference between the predicted and the actual values is considered to be the contribution of solid solution strengthening. The yield strength is most significantly influenced by grain boundary strengthening and dislocation strengthening, while solid solution strengthening has the least impact. As the extrusion temperature decreases, the grains become smaller and the density of residual dislocations increases significantly. The ZS-290 alloy exhibits the highest strength due to its small grain size and high density of the residual dislocations.

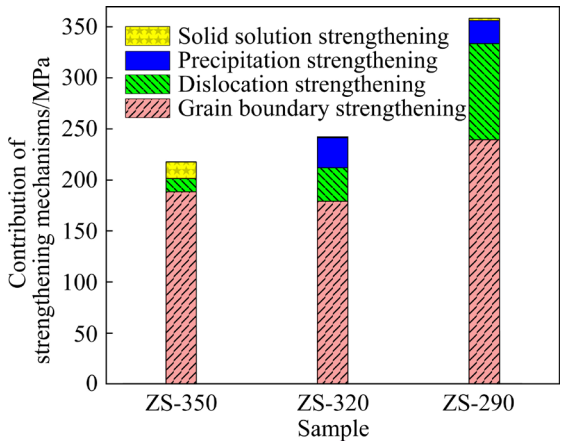

Fig. 13 Contributions of different strengthening mechanisms of ZS-350, ZS-320, and ZS-290 alloys

4.2.2 Plasticity mechanism

In the analysis of the mechanical properties of the ZS-350, ZS-320, and ZS-290 alloys in relation to the change of extrusion temperatures, it is observed that as the extrusion temperature decreases, the elongation decreases. Further investigation into the plasticity mechanism is conducted. Figure 14 shows the SEM images of tensile-fractured morphologies of ZS-350, ZS-320, and ZS-290 alloys. The fracture surfaces of all three alloys exhibit dissociation surfaces and broken second phase particles, indicating a common mode of failure (Figs. 14(a, c, e)). Additionally, twins are observed in the microstructure near the fractures (Figs. 14(b, d, f)). LI et al [4] reported that the plasticity of the alloys is influenced by the types, volume fractions, and sizes of the second phase particles. However, in the case of the three experimental alloys in this work, the types and volume fractions of the second phase particles remain unaffected by the extrusion temperature (Fig. 6). Additionally, the sizes of the second phase particles are only slightly affected by the extrusion temperature (Fig. 5). Consequently, the decrease in plasticity observed cannot be solely attributed to the second phase particles.

Twins can indeed have a significant effect on the plasticity of the alloys, and coarse twins can act as the crack initiation sites during the tensile deformation, leading to fracture and reduced plasticity [31,32]. It is observed that twins are present in the coarse unDRXed grains but not in the fine DRXed grains. Some twins exhibit cracks (Fig. 14(f)), indicating that the twins serve as locations for crack initiation, thereby diminishing the overall plasticity of the alloy. Figure 15 shows the Schmid factor distributions of $\{10\bar{1}2\}$ tensile twin of unDRXed grains in the ZS-350, ZS-320,

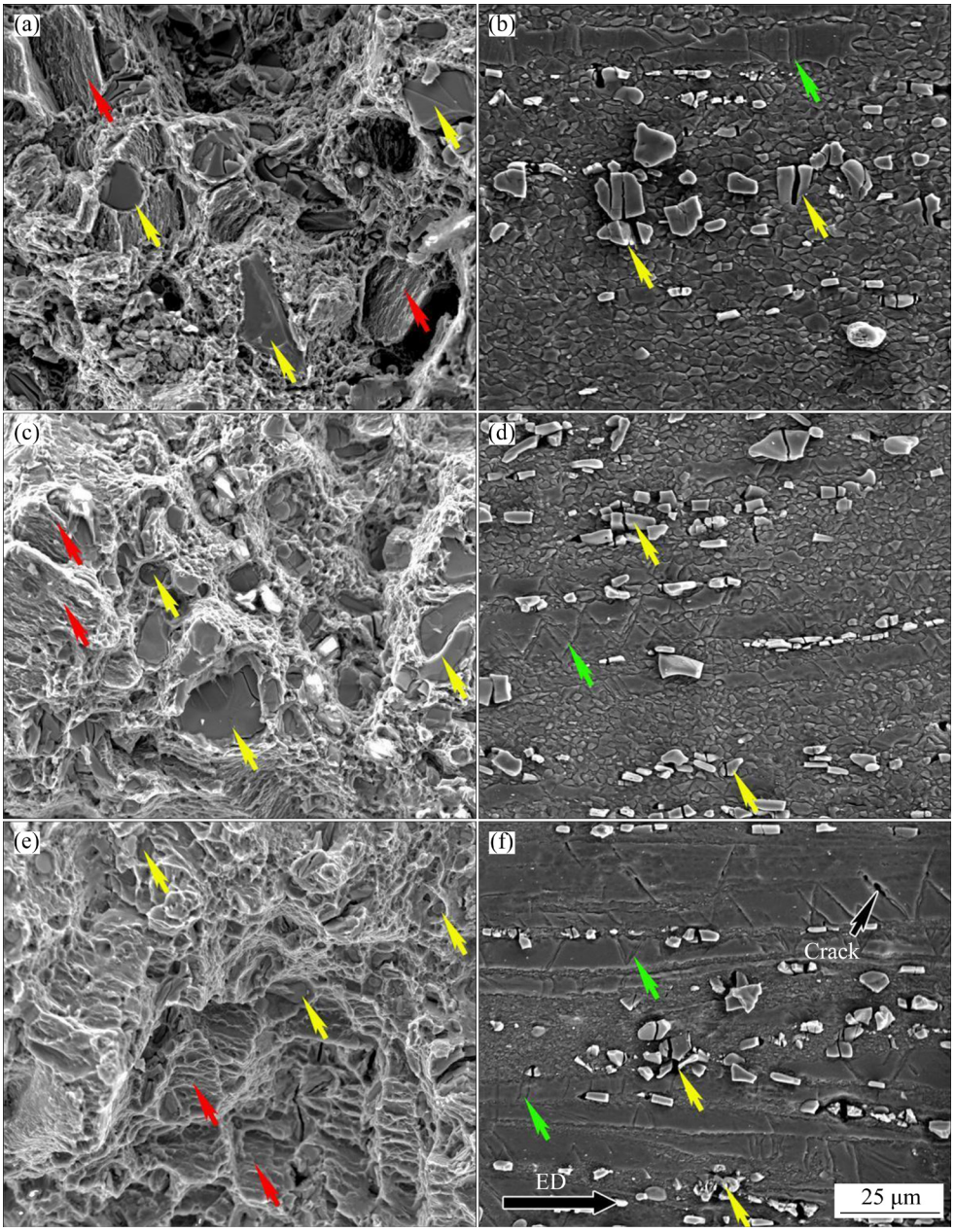

Fig. 14 SEM images of tensile-fractured morphologies of ZS-350 (a, b), ZS-320 (c, d), and ZS-290 (e, f) alloys (Red arrows represent dissociation surfaces, yellow arrows represent broken second phase particles, and green arrows represent twins)

and ZS-290 alloys. The Schmid factors of $\{10\bar{1}2\}$ tensile twins of unDRXed grains of ZS-350, ZS-320, and ZS-290 alloys are 0.48, 0.47, and 0.48, respectively, being very close to 0.5. Therefore, the type of twins can be determined to be $\{10\bar{1}2\}$ tensile twin. The volume fraction of unDRXed grains increases as the extrusion temperature decreases (Fig. 1). The increase in the volume fraction of unDRXed grains leads to an increase in the number of $\{10\bar{1}2\}$ tensile twins during the tensile deformation, resulting in a decrease in plasticity. Therefore, it can be concluded that the plasticity of the ZS-290 alloy is the worst due to its highest volume fraction of unDRXed grains.

5 Conclusions

(1) The alloy demonstrates excellent flame-retardant performance and does not burn at 1058 °C. The alloy has a bimodal microstructure consisting of coarse unDRXed grains elongated along the extrusion direction and fine DRXed grains. The

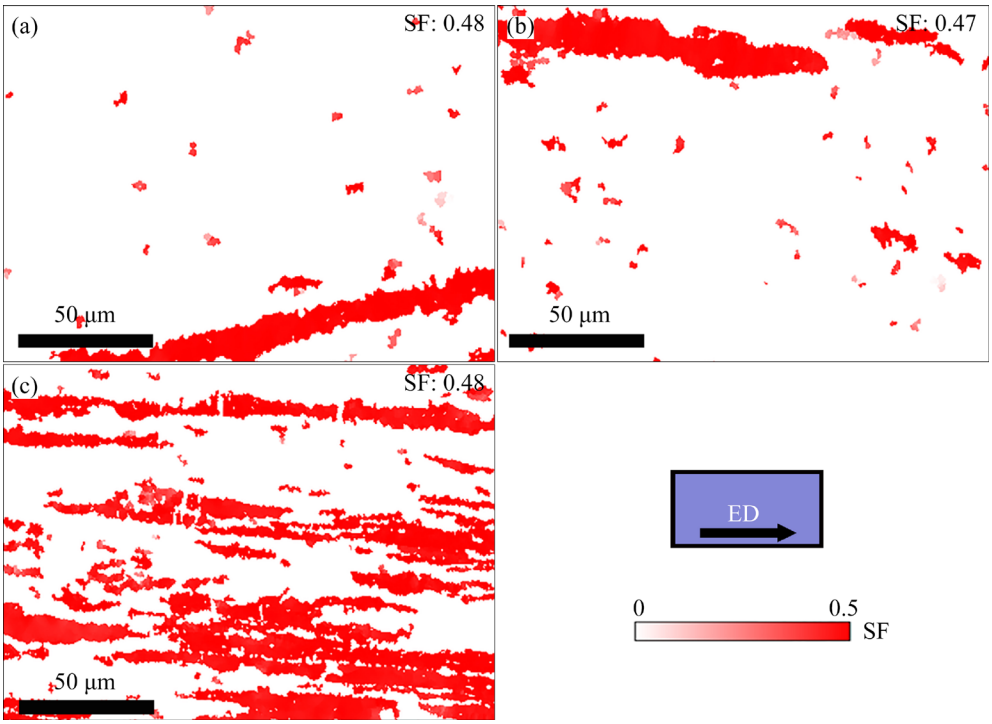

Fig. 15 Schmid factor (SF) distributions of $\{10\bar{1}2\}$ tensile twins of unDRXed grains of ZS-350 (a), ZS-320 (b), and ZS-290 (c) alloys

volume fraction of DRXed grains decreases as the extrusion temperature decreases.

(2) The dynamic recrystallization mechanisms of alloy are continuous dynamic recrystallization (CDRX) mechanism and particle simulated nucleation (PSN) mechanism during hot extrusion.

(3) As the extrusion temperature decreases from 350 to 290 °C, the yield strength increases significantly from 218 to 358 MPa, representing a rise of approximately 70%. This notable enhancement in strength is primarily attributed to grain boundary strengthening and dislocation strengthening mechanisms.

(4) The volume fraction of unDRXed grains increases as the extrusion temperature decreases. The increase in the volume fraction of unDRXed grains results in a higher occurrence of $\{10\bar{1}2\}$ tensile twins during the tensile deformation, subsequently leading to a reduction in plasticity.

CRediT authorship contribution statement

Xi-zao WANG: Methodology, Investigation, Data curation, Writing − Original draft; **Tian-jiao LUO:** Writing − Review & editing, Funding acquisition; **Qiu-yan HUANG:** Methodology; **Tian-yu LIU:** Methodology, Writing − Review & editing; **Ying-ju LI:** Writing − Review & editing; **Ce ZHENG:** Writing − Review & editing; **Shuang GUO:** Writing − Review & editing; **Yuan-sheng YANG:** Supervision, Methodology.

Declaration of competing interest

The authors declare that they have no known competing financial interests or personal relationships that could have appeared to influence the work reported in this paper.

Acknowledgments

This work was supported by the National Key Research and Development Program of China (No. 2021YFB3701100), the Applied Basic Research Program Project of Liaoning Province, China (No. 2023020253-JH2/1016), and the Key Research and Development Plan of Shanxi Province, China (No. 202102050201005).

References

[1] HAN Dong, ZHANG Jin, HUANG Jin-feng, LIAN Yong, HE Guang-yu. A review on ignition mechanisms and characteristics of magnesium alloys [J]. Journal of Magnesium and Alloys, 2020, 8: 329−344.

[2] NI Jing, JIN Li, ZENG Jian, LI Jing, WANG Fu-lin, WANG Feng-hua, DONG Shuai, DONG Jie. Development of high-strength magnesium alloys with excellent ignition-proof

performance based on the oxidation and ignition mechanisms: A review [J]. Journal of Magnesium and Alloys, 2023, 11: 1−14.

[3] XU S W, OHISHI K, KAMADO S, UCHIDA K, HOMMA H, HONO K. High-strength extruded Mg−Al−Ca−Mn alloy [J]. Scripta Materialia, 2011, 65: 269−272.

[4] LI Z T, QIAO X G, XU C, LIU X Q, KAMADO S, ZHENG M Y. Enhanced strength by precipitate modification in wrought Mg−Al−Ca alloy with trace Mn addition [J]. Journal of Alloys and Compounds, 2020, 836: 154689.

[5] WANG Xiao-yuan, WANG Fei-yu, WANG Cheng, XU Shun, RONG Jian, YANG Zhi-zheng, WANG Jin-Guo, WANG Hui-yuan. A simultaneous improvement of both strength and ductility by Sn addition in as-extruded Mg−6Al−4Zn alloy [J]. Journal of Materials Science & Technology, 2020, 49: 117−125.

[6] HUANG Yu-chuan, ZHANG Quan-da, OUYANG Si-jie, SUN Fu-zhen, SUN Jia-wei, LI Hui-yu, WU Guo-hua, CHEN Pei-jun, LIU Wen-cai. Effects of Zn and Gd contents and their ratios on microstructure and mechanical properties of as-cast and as-extruded Mg−8Li alloys [J]. Transactions of Nonferrous Metals Society of China, 2024, 34: 798−811.

[7] JANG H S, LEE B J. Effects of Zn on ⟨*c*+*a*⟩ slip and grain boundary segregation of Mg alloys [J]. Scripta Materialia, 2019, 160: 39−43.

[8] BIAN Ming-zhe, HUANG Xin-sheng, CHINO Y. Substantial improvement in cold formability of concentrated Mg−Al−Zn−Ca alloy sheets by high temperature final rolling [J]. Acta Materialia, 2021, 220: 117328.

[9] BIAN M Z, SASAKI T T, SUH B C, NAKATA K, KAMADO S, HONO K. A heat-treatable Mg−Al−Ca−Mn−Zn sheet alloy with good room temperature formability [J]. Scripta Materialia, 2017, 138: 151−155.

[10] HOSEINIATHAR M M, MAHMUDI R, PRASATH B, HEDSTROM P. Effect of Zn addition on dynamic recrystallization behavior of Mg−2Gd alloy during high-temperature deformation [J]. Journal of Alloys and Compounds, 2019, 806: 1200−1206.

[11] LIU Lin-tao, BAI Sheng-wen, JIANG Bin, HE Chao, WANG Qing-hang, ZHOU Jian-xin, WEI Li-ping, QIAN Xiao-ying, DONG Zhi-hua, HUANG Guang-sheng, ZHANG Ding-fei, PAN Fu-sheng. Achieving preeminent strength-ductility synergy of Mg−1Sb−1Mn alloy via trace co-addition of Sn and Zn [J]. Materials Science and Engineering A, 2023, 862: 144431.

[12] TRANG T T, ZHANG J H, KIM J H, ZARGARAN A, WANG J H, SUH B C, KIM N J. Designing a magnesium alloy with high strength and high formability [J]. Nature Communications, 2018, 9: 2522.

[13] AMITAVA M, SEONG G K, HORSTEMEYER M F. Solute effect on the ⟨*c*+*a*⟩ dislocation nucleation mechanism in magnesium [J]. Acta Materialia, 2014, 75: 106−112.

[14] WU Xiao-feng, XU Chun-xiang, ZHANG Zheng-wei, YANG Wen-fu, ZHANG Jing-shan. Microstructure evolution, strengthening mechanisms and deformation behavior of high-ductility Mg−3Zn−1Y−1Mn alloy at different extrusion temperatures [J]. Transactions of Nonferrous Metals Society of China, 2023, 33: 422−437.

[15] LIU Shuai-shuai, LIU Han, ZHANG Bao-xuan, HUANG Guang-sheng, CHEN Xiang, TANG Ai-tao, JIANG Bin, PAN Fu-sheng. Effects of extrusion temperature on microstructure evolution and mechanical properties of heterogeneous Mg−Gd alloy laminates via accumulated extrusion bonding [J]. Transactions of Nonferrous Metals Society of China, 2022, 32: 2190−2204.

[16] LV Hao, LI Lu, WEN Zhuo-zhang, LIU Chun-rong, ZHOU Wei, BAI Xue, ZHONG Hui-ling. Effects of extrusion ratio and temperature on the microstructure and mechanical properties of Mg−Zn−Yb−Zr extrusion alloys [J]. Materials Science and Engineering A, 2022, 833: 142521.

[17] CHA J W, PARK S H. Variations in dynamic recrystallization behavior and mechanical properties of AZ31 alloy with extrusion temperature [J]. Journal of Magnesium and Alloys, 2023, 11: 2351−2365.

[18] YANG Zhao, XU Chao, NAKATA T, KAMADO S. Effect of extrusion ratio and temperature on microstructures and tensile properties of extruded Mg−Gd−Y−Mn−Sc alloy [J]. Materials Science and Engineering A, 2021, 800: 140330.

[19] LI Z T, ZHANG X D, ZHENG M Y, QIAO X G, WU K, XU C, KAMADO S. Effect of Ca/Al ratio on microstructure and mechanical properties of Mg−Al−Ca−Mn alloys [J]. Materials Science and Engineering A, 2017, 682: 423−432.

[20] LI Z T, QIAO X G, XU C, KAMADO S, ZHENG M Y, Luo A A. Ultrahigh strength Mg−Al−Ca−Mn extrusion alloys with various aluminum contents [J]. Journal of Alloys and Compounds, 2019, 792: 130−141.

[21] PAN Hu-cheng, QIN Gao-wu, HUANG Yun-miao, REN Yu-ping, SHA Xue-chao, HAN Xiao-dong, LIU Zhi-quan, LI Cai-fu, WU Xiao-lei, CHEN Hou-wen, HE Cong, CHAI Lin-jiang, WANG Yun-zhi, NIE Jian-feng. Development of low-alloyed and rare-earth-free magnesium alloys having ultra-high strength [J]. Acta Materialia, 2018, 149: 350−363.

[22] XU Jun, JIANG Bin, SONG Jiang-feng, HE Jun-jie, GAO Peng, LIU Wen-jun, YANG Tian-hao, HUANG Guang-sheng, PAN Fu-sheng. Unusual texture formation in Mg−3Al−1Zn alloy sheets processed by slope extrusion [J]. Materials Science and Engineering A, 2018, 732: 1−5.

[23] HUANG Wei-ying, CHEN Jian-hua, JIANG Zhen, XIONG Xi, QIU Wei, CHEN Jian, REN Xian-wei, LU Li-wei. Influence of Ca Content on Microstructure and Mechanical Properties of Extruded Mg−Al−Ca−Mn Alloys [J]. Acta Metallurgica Sinica (English Letters), 2022, 36:426−438.

[24] HUANG Qiu-yan, LIU Yang, TONG Min, PAN Hu-cheng, YANG Chang-lin, LUO Tian-jiao, YANG Yuan-sheng. Enhancing tensile strength of Mg−Al−Ca wrought alloys by increasing Ca concentration [J]. Vacuum, 2020, 177: 109356.

[25] LI J R, XIE D S, ZENG Z R, SONG B, XIE H B, PEI R S, PAN H C, REN Y P, QIN G W. Mechanistic investigation on Ce addition in tuning recrystallization behavior and mechanical property of Mg alloy [J]. Journal of Materials Science & Technology, 2023, 132: 1−17.

[26] HUANG Ying-jie, WAN Ying-chun, LIU Chu-ming, JIANG Shu-nong, GAO Yong-hao, CHEN Zhi-yong. Effect of forging temperature on the microstructure, subsequent aging precipitation behavior, and mechanical properties of Mg−Gd−Y−Zr−Ag alloy [J]. Journal of Materials Science &

Technology, 2024, 181: 41−57.
[27] PAN Hu-cheng, KANG Rui, LI Jing-ren, XIE Hong-bo, ZENG Zhuo-ran, HUANG Qiu-yan, YANG Chang-lin, REN Yu-ping, QIN Gao-wu. Mechanistic investigation of a low-alloy Mg−Ca-based extrusion alloy with high strength−ductility synergy [J]. Acta Materialia, 2020, 186: 278−290.
[28] LIU Xuan, ZHANG Zhi-qiang, HU Wen-yi, LE Qi-chi, BAO Lei, CUI Jian-zhong. Effects of extrusion speed on the microstructure and mechanical properties of Mg9Gd3Y1.5Zn0.8Zr alloy [J]. Journal of Materials Science & Technology, 2016, 32: 313−319.
[29] LUO P, MCDONALD D T, XU W, PALANISAMY S, DARGUSCH M S, XIA K. A modified Hall−Petch relationship in ultrafine-grained titanium recycled from chips by equal channel angular pressing [J]. Scripta Materialia, 2012, 66: 785−788.
[30] NIE J F. Effects of precipitate shape and orientation on dispersion strengthening in magnesium alloys [J]. Scripta Materialia, 2003, 48: 1009−1015.
[31] WANG Qing-hang, ZHAI Hao-wei, LIU Lin-tao, XIE Hong-bo, JIANG Bin, ZHAO Jun, CHEN Dao-lun, PAN Fu-sheng. Novel Mg−Bi−Mn wrought alloys: The effects of extrusion temperature and Mn addition on their microstructures and mechanical properties [J]. Journal of Magnesium and Alloys, 2022, 10: 2588−2606.
[32] JIN S C, LEE J, JONG G, YU Hui, PARK S H. Effects of Sn addition on the microstructure and mechanical properties of extruded Mg−Bi binary alloy [J]. Journal of Magnesium and Alloys, 2022, 10: 850−861.

挤压温度对阻燃 Mg−Al−Ca−Zn−Sn−Mn 合金动态再结晶行为和力学性能的影响

王锡灶[1,2]，罗天骄[1]，黄秋燕[1]，刘天宇[1,2]，李应举[1]，郑 策[1]，郭 爽[1,3]，杨院生[1]

1. 中国科学院 金属研究所，沈阳 110016；
2. 中国科学技术大学 材料科学与工程学院，沈阳 110016；
3. 沈阳工业大学 材料科学与工程学院，沈阳 110870

摘 要：研究了挤压温度对阻燃 Mg−6Al−3Ca−1Zn−1Sn−Mn(质量分数，%)合金动态再结晶行为和力学性能的影响。热挤压过程中合金的动态再结晶机制为连续动态再结晶(CDRX)和颗粒诱导形核(PSN)。通过降低挤压温度，屈服强度从 218 MPa 显著提高到 358 MPa，提高了 140 MPa。对强化机制进行了定量分析，强度的提高主要归因于晶界和位错强化。对塑性机理进行了定性分析，降低挤压温度，未再结晶晶粒体积分数的增加导致拉伸变形过程中$\{10\bar{1}2\}$拉伸孪晶数量的增加，从而降低了塑性。

关键词：阻燃镁合金；PSN 机制；高强度；热挤压

(Edited by Bing YANG)